Journal of Power Sources 189 (2009) 1220–1230

Contents lists available at ScienceDirect

Journal of Power Sources

journal homepage: www.elsevier.com/locate/jpowsour

Numerical modelling of a bromide–polysulphide redox flow battery Part 1: Modelling approach and validation for a pilot-scale system

Daniel P. Scamman[a], Gavin W. Reade[b,1], Edward P.L. Roberts[a,*,2]

[a] School of Chemical Engineering and Analytical Science, University of Manchester, Sackville St, PO Box 88, Manchester M60 1QD, UK
[b] Regenesys Technologies Limited, OTEF, Aberthaw Power Station, Barry, Vale of Glamorgan CF62 4QT, UK

ARTICLE INFO

Article history:
Received 2 December 2008
Received in revised form 22 January 2009
Accepted 25 January 2009
Available online 6 February 2009

Keywords:
Redox flow battery
Numerical model
Bromide–polysulphide
Electrochemical rate constant

ABSTRACT

Numerical modelling of redox flow battery (RFB) systems for energy storage applications allows the technical performance of different designs to be predicted without costly lab, pilot and full-scale testing. A one-dimensional numerical model has been developed for RFB systems with bipolar flow-by electrodes, soluble redox couples, and recirculating batch operation. Overpotential losses were estimated from the Butler-Volmer equation, accounting for mass transfer. The effects of cross-membrane solvent transport and self-discharge were also considered. The model predicted the variation in concentration and current along the electrode and determined the charge–discharge efficiency, energy density and power density. The model was validated using data obtained from a pilot-scale bromide–polysulphide (PSB) system commercialised by Regenesys Technologies (UK) Ltd. Electrochemical rate constants were obtained by fitting the model results to the experimental data, and values of 4×10^{-7} and 3×10^{-8} m s^{-1} were found for the bromide and sulphide electrolytes on the activated carbon electrodes. The model was able to predict cell performance, species concentration, current distribution and electrolyte deterioration for the Regenesys system.

1. Introduction

The demand for utility-scale energy storage is growing due to an increasing need for load-smoothing to allow the decommissioning of old power plant, to improve power quality for the growing digital economy, to improve security of supply through black-start capability and to smooth the output from renewable energy technologies. Redox flow batteries (RFBs) have been investigated for many years as chemical stores of electrical energy [1,2], and are the closest storage technology to widespread commercialisation [3]. RFBs have numerous advantages over other batteries, including a separation of the energy and power rating, modular systems, repeatable cyclic behaviour and the use of benign chemicals at atmospheric temperature and pressure. Redox couples currently under development for use in RFBs include polysulphide–bromine (PSB) [4–7], vanadium–vanadium [8,9], vanadium–polyhalide [10], cerium–zinc [11–13] and lead–lead [2]. Numerical modelling of redox flow battery systems for energy storage applications allows the technical and commercial performance of different designs to be predicted without costly lab, pilot and full-scale testing. Limited modelling of RFB systems has been carried out to date. A study of the iron–chromium system included reaction kinetics, mass transfer, ohmic losses and hydrogen evolution, and found an optimum electrode thickness and electrolyte flow rate [14]. A model of the zinc-ferricyanide couple considered only mass-transport-limited conditions [15]. An investigation of the bromide half-couple found that a couple of reaction mechanisms could account for observed behaviour [16]. A review of modelling work on the zinc–bromide system has reported recommendations for improving cell design [17].

In this paper we develop a numerical model of a RFB system, and apply this to the Regenesys Technologies Ltd. pilot-scale PSB-based RFB. The PSB RFB has not previously been studied by numerical simulation. Numerical modelling can be used to obtain key parameters such as the electrochemical rate constants for the reactions. Furthermore, once validated, the model can be used to evaluate and optimise the design and performance of a full-scale commercial RFB system. This is the subject of a following paper [18].

2. Method

2.1. Cell layout

The model centred on a single, vertical, membrane-divided regenerative electrochemical cell as shown in Fig. 1. The electrolytes entered at the bottom of the cell (to allow easy filling, promote

* Corresponding author. Tel.: +44 161 306 8849; fax: +44 161 306 9321.
E-mail address: Edward.roberts@manchester.ac.uk (E.P.L. Roberts).
[1] Present address: Rolls Royce plc, PO Box 31, Derby DE24 8BJ, UK.
[2] ISE Member.

0378-7753/$ – see front matter © 2009 Elsevier B.V. All rights reserved.
doi:10.1016/j.jpowsour.2009.01.071

Nomenclature

Nomenclature

A	electrode area (m^2 cell^{-1})
A_{Chan}	channel flow area (m^2 cell^{-1})
d_e	electrode hydraulic diameter (m)
D	diffusion coefficient (m^2 s^{-1})
E	voltage (V)
E^0	standard potential (V)
F	Faraday's constant (96,485 C mol^{-1})
H	number of segments
I	current (A)
i	current density (A m^{-2})
i_0	exchange current density (A m^{-2})
i_d	dimensionless current i/i_L
i_L	limiting current density (A m^{-2})
i_{Lr}	limiting current ratio
i_r	current ratio
J	species flux across the membrane (mol m^{-2} s^{-1})
k_m	mass transfer coefficient (m s^{-1})
k_s	kinetic rate constant (m s^{-1})
N	number of cells
N_{it}	number of iterations
O	oxidised species*
$[P]$	concentration of species P (mol dm^{-3})
R	reduced species*
R	universal gas constant (8.314 J mol^{-1} K^{-1})
R	resistance (Ω)
l	thickness (m)
t	time (s)
Δt	time increment (s)
T	temperature (K)
T_{comp}	computational time (s)
v	electrolyte velocity (m s^{-1})
V	electrolyte volume (m^3)
z	number of electrons transferred per occurrence of overall reaction*
z_P	stoichiometric coefficients of species P

Greek symbols

α	charge transfer coefficient
ε	relative error
η	overpotential (V)
η_f	dimensionless overpotential
κ	conductivity (S m^{-1})
λ_h	convergence criterion of segment iteration (A m^{-2})
λ_e	convergence criterion of electrode iteration (V)
ν	kinematic viscosity (m^2 s^{-1})
σ	state of charge

Subscripts

a	anodic value
A	half-couple A
ave	average value
B	half-couple B
Br	value for the bromide electrolyte
bulk	value in electrolyte bulk
c	cathodic value
CELL	cell value
ch	value on charge cycle
dis	value on discharge cycle
entry	value at electrode entry
eqm	equilibrium value
exit	value at electrode exit
Est	estimated value
f	value for forward reaction
h	segment value
M	membrane
P	value for general species P
S	value for the sulphide electrolyte
T	tank value

Dimensionless numbers

Re	Reynolds number (vd_e/ν)
Sc	Schmidt number (ν/D)
Sh	Sherwood number ($k_m d_e/D$)

good mixing and even conditions across the cell, and allow gases to escape easily), were pumped upwards where the dissolved active species reacted at flow-by electrodes, and left at the top to be stored in tanks. On charge, redox couple A was oxidised at the anode and couple B was reduced at the cathode while cations crossed the membrane to maintain electro-neutrality, with the reverse occurring on discharge. Multiple cells were connected together in parallel using bipolar electrodes to form stacks, and electrolytes were fed into and collected from the cell using manifolds. The same tank was used to store the reactants and products, so that the electrolytes recirculated with the concentration of product steadily increasing over time. A constant current was supplied, and the cell voltage changed during the charging cycle as the concentrations of reactants and products varied.

2.2. Model scope and assumptions

The RFB numerical model developed in this paper performed the following functions:

- Evaluation of mass transport (from the electrolyte bulk to the electrode surface) and reaction kinetics (described by the Butler-Volmer equation with 1st-order reaction rates and equal rate constants for anodic and cathodic processes) as rate-determining processes.
- Estimation of the variation in concentration, overpotential, current density, exchange current density and limiting current density up the electrode in a one-dimensional model.
- Calculation of the variation in cell performance during charge–discharge cycles and overall system characteristics including energy efficiency, power density and energy density.
- Consideration of different operating conditions and electrolyte systems, *e.g.* variable redox couple, applied current density, power rating, operating temperature, catalyst, cycle length, species concentration, electrolyte velocity, electrode area, stack size, tank volume, electrolyte conductivity and membrane conductivity.
- Estimation of the effect of the diffusion of electro-active species and electro-osmotic flow of water across the membrane.

The main assumptions used in the model are listed below:

- Single-step electrochemical reactions involving dissolved electro-active species were assumed to occur at the electrodes.
- Electrochemical kinetics were assumed to be described by the Butler-Volmer equation, with the anodic and cathodic charge transfer coefficients summing to one.
- Electrochemical rate constants and mass transfer coefficients were assumed to be approximately constant, *i.e.* the effect of temperature, electrode-fouling, *etc.* was not included.

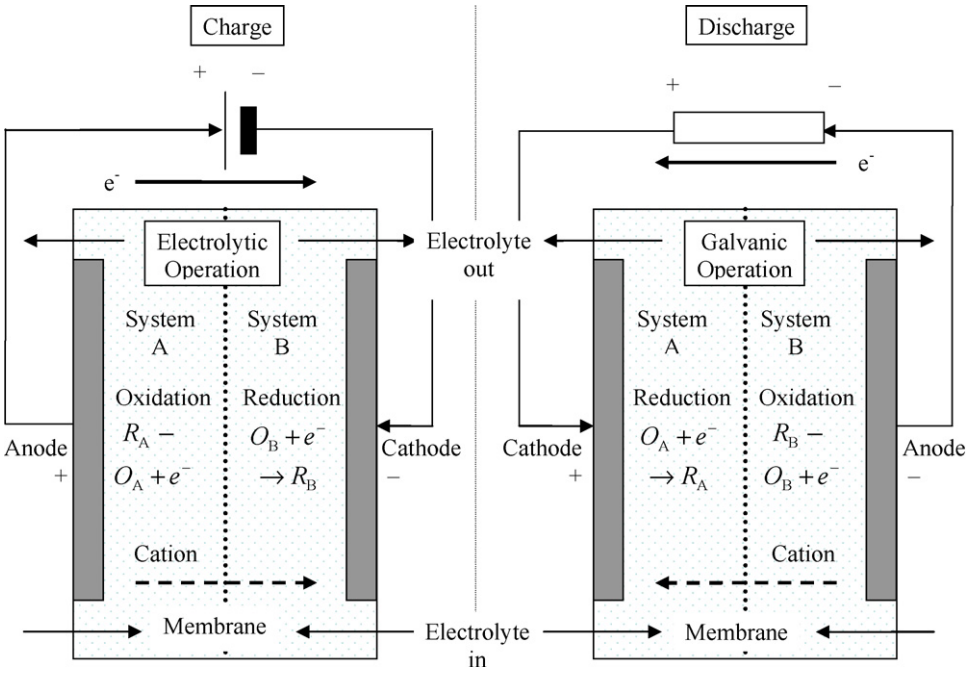

Fig. 1. Cell layout and electrochemical conventions.

- The effects of electro-migration and mass transport away from the electrode were assumed to be negligible.
- The effects of adsorption, capacitance, electrodes/endplates resistivity and shunt currents were assumed to be negligible.
- The current efficiency was assumed to be 100%, *i.e.* side reactions were not considered.
- Plug flow conditions were assumed to occur in the cells, with a constant electrolyte velocity in both half-cells and during cycles.
- Conditions were assumed to be the same in each cell in a stack, so that the performance of a stack of cells could be determined directly from the performance of a single cell.

2.3. Model equations

The model assumed that simple, single-step, single-species electrochemical reactions occurred at each electrode:

$$z_O O + ze^- \leftrightharpoons z_R R \tag{1}$$

The cell voltage was calculated from equilibrium potentials at the electrodes, accounting for the main losses in the cell. During charging the cell voltage was calculated as:

$$E_{CELL} = E_{eqm,A} - E_{eqm,B} + \eta_A - \eta_B + (IR_A + IR_B + IR_M) \tag{2}$$

On discharging, the cell voltage was calculated as:

$$E_{CELL} = E_{eqm,A} - E_{eqm,B} + \eta_A - \eta_B - (IR_A + IR_B + IR_M) \tag{3}$$

The equilibrium potentials at each electrode, $E_{eqm,A}$ and $E_{eqm,B}$ were derived from the standard potential and species concentrations (assuming unit activity coefficients) as given in the Nernst equation:

$$E_{eqm} = E^0 - \frac{RT}{zF} \ln \frac{[R]^{z_R}}{[O]^{z_O}} \tag{4}$$

The electrolyte and membrane resistances R_A, R_B and R_M were derived from:

$$R = \frac{l}{\kappa A} \tag{5}$$

where l is the thickness (membrane or electrolyte), κ is the conductivity and A is the active area of the electrode. The overpotentials η resulting at each electrode was determined by inverting the Butler-Volmer equation, accounting for the effect of mass transport on the active species concentration at the electrode:

$$i = \frac{\exp\{(\alpha_a zF/RT)\eta\} - \exp\{-(\alpha_c zF/RT)\eta\}}{(1/i_0) + (1/i_{La})\exp\{(\alpha_a zF/RT)\eta\} - (1/i_{Lc})\exp\{-(\alpha_c zF/RT)\eta\}} \tag{6}$$

where the exchange current density i_0, anodic limiting current density i_{La}, and cathodic limiting current density i_{Lc} were defined as:

$$i_0 = zFk_s[O]_{bulk}^{\alpha_a}[R]_{bulk}^{\alpha_c} \tag{7}$$

$$i_{La} = zFk_{m,R}[R]_{bulk} \tag{8}$$

$$i_{Lc} = -zFk_{m,O}[O]_{bulk} \tag{9}$$

In Eqs. (6)–(9), both z_O and z_R equal 1. No adequate rate expression is currently known for electrochemical reactions with values for z_O and z_R other than 1, and it has been observed that complex reaction mechanisms often show simple behaviour and can be treated by relations of this sort [19]. It is likely that values of z_O and z_R other than 1 will affect the scaling but not the form of the Butler-Volmer equation, and hence it is reasonable to neglect their influence on Eqs. (6)–(9).

The inversion of Eq. (6) was achieved using approximations to the Butler-Volmer equation rather than iteration in order to reduce computational time. Eq. (6) was written in dimensionless format:

$$i_{df} = \left|\frac{i_f}{i_{Lf}}\right| = \frac{\exp\{\alpha_f\eta_f\} - \exp\{-(1-\alpha_f)\eta_f\}}{i_{rf} + \exp\{\alpha_f\eta_f\} + i_{Lr}\exp\{-(1-\alpha_f)\eta_f\}} \tag{10}$$

The forward process was either anodic or cathodic depending on the direction of the net reaction. The dimensionless current i_{df} varied between 0 and +1 and gave a simple indication of the nearness of the current to mass-transport limits. Other dimensionless quantities were defined as:

$$\eta_f = \left|\frac{zF}{RT}\eta\right| \tag{11}$$

$$i_{rf} = \left|\frac{i_{Lf}}{i_0}\right| \tag{12}$$

$$i_{Lr} = \left|\frac{i_{Lf}}{i_{Lb}}\right| \tag{13}$$

The current ratio (i_{rf}) gave an indication of the relative rates of mass transport and reaction kinetics. Eqs. (10) and (11) define the dimensionless overpotential η_f as a function of four positive quantities: i_{df}, α_f, i_{rf} and i_{Lr}.

Three approximations were used to invert Eq. (10): the Linear, mass-transport-limited (MTL) Tafel and Sigmoidal approximations:

$$\eta_f = i_{rf} i_{df} \tag{14}$$

$$\eta_f = \frac{1}{\alpha_f} \ln\left[\frac{i_{rf} i_{df}}{1 - i_{df}}\right] \tag{15}$$

$$\eta_f = \ln\left[\frac{1 + i_{Lr} i_{df}}{1 - i_{df}}\right] \tag{16}$$

The Linear approximation was used for conditions of low i_{df}, the MTL Tafel approximation in conditions of high i_{df}, and the Sigmoidal approximation in conditions of low i_{rf}. Further details of the inversion method are described elsewhere [20], where it has been shown that the error in overpotential obtained from using these approximations was of the order of 10^{-5}. At the transition points between the approximations the error could rise to around 10%, although the resulting error in derived quantities such as cell voltage and time-averaged quantities such as current efficiency would be much less than this.

2.4. Model methodology

The model methodology is shown in Fig. 2. First, the cell voltage E_{Est} (assumed to be constant up the electrode length) was estimated. A one-dimensional numerical model of the current distribution along the electrode was calculated by dividing the electrode into H segments and calculating the current in each segment iteratively. The current i_h in an individual segment was estimated, and used to find the species exit concentrations. In each segment the species concentrations, equilibrium potentials $E_{eqm,A}$ and $E_{eqm,B}$, overpotentials η_A and η_B and the ohmic losses in the electrolyte and membrane were calculated. The segment voltage E_h was calculated from Eqs. (2) and (3), and an interpolation-bisection iteration of i_h was carried out until the discrepancy between E_h and E_{Est} fell below a segment convergence criterion λ_h. This iteration was repeated for all the segments along the electrode, and the average current density i_{ave} found from the resulting current distribution. A second iteration was performed, varying E_{Est} until the discrepancy between i_{ave} and i_{CELL} was less than an electrode convergence criterion λ_e. This gave the cell voltage E_{CELL} at time t. The above calculation process was repeated for the length of the charging cycle and for subsequent charging and discharging cycles using Faraday's law and a mass balance to calculate the concentration of the electrolytes in the storage tanks.

Both of the iteration loops in the model were executed using an interpolation-bisection method. Bisection methods converge as long as initial limits are chosen either side of the solution, and as the voltage–current relationship in the mixed kinetic-limited/mass-transport-limited region of the Butler-Volmer equation frequently encountered in this study is approximately linear, linear interpolation was found to converge quickly.

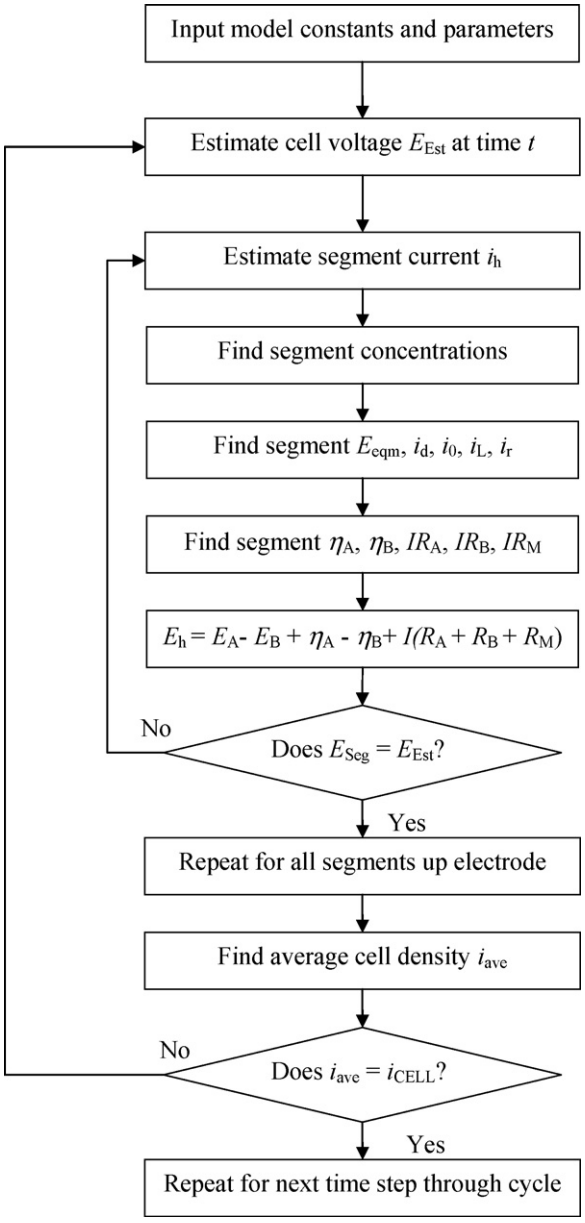

Fig. 2. Flowchart of numerical redox flow battery model.

3. The bromide–polysulphide couple

For long-term storage, high solubility, low toxicity and low cost salts are needed and alkali metal salts of bromine, chlorine and sulphur are ideal. These salts are attractive due to their abundance and availability at the necessary degree of purity at moderate cost. The sodium bromide–polysulphide redox couple is attractive for flow batteries because it presents no adverse hazards in handling or storage in its uncharged state, whereas other redox couples are not as suitable for reasons of safety, efficiency and cost [5]. Bromine has long been investigated as an electrolyte for redox flow batteries, normally with zinc as the other electro-active species [21,22], and the PSB couple avoids the problem of handling deposited solid metal. The high stability of the bromide ion gives it a high potential, making it attractive for redox flow batteries. Bromine is only sparingly soluble in water but does complex as soluble tribromide ions Br_3^-, and this increases its solubility at room temperatures. Polysulphide has not been considered as an electrolyte as extensively as bromide. The dissolved sulphur appears as polysulphide ions with a maximum chain length of five sulphur atoms, and usually as S_4^{2-} or S_5^{2-} ions. The maximum solubility of K_2S is 8.8 M K_2S at 25 °C, which corresponds to 2.2 M K_2S_4 when discharged [23]. This ability to store large amounts of dissolved zero-valent sulphur as polysulphides means that sulphur solutions are good catholytes [24]. The standard potential for the bromide and polysulphide reactions are +1.087 and −0.508 V respectively, giving an overall standard potential of 1.59 V. This is close to the maximum achievable in water-based systems of about 2 V, but means that gas evolution occurs at both high and low states of charge. The state of

charge of each electrolyte was defined as:

$$\sigma_{Br} = \frac{[Br_2]}{[Br_2] + \frac{1}{2}[Br^-]} \quad (17)$$

$$\sigma_S = \frac{[S^{2-}] - \frac{1}{4}[S]}{[S^{2-}] + [S]} \quad (18)$$

Here [S] refers to the total concentration of zero-valent sulphur. These expressions are independent of electrolyte volume. The fresh electrolytes consisted of 3.8 m^3 of 4.5 M NaBr and 3.2 m^3 of 1.0 M $Na_2S_{4.8}$, with V_{Br} greater than V_S to allow for cross-membrane water transport. It can be simply shown that, for these fresh compositions, σ_{Br} and σ_S are linked by [20]:

$$\sigma_S = \frac{75}{128}\sigma_{Br} + \frac{1}{96} \quad (19)$$

The conductivities and viscosities of the electrolytes have been determined at 35 °C and at mid-charge: $\kappa_{Br} = 23\ S\ m^{-1}$, $\kappa_S = 29\ S\ m^{-1}$, $\nu_{Br} = 0.76 \times 10^{-6}\ m^2\ s^{-1}$ and $\nu_S = 1.18 \times 10^{-6}\ m^2\ s^{-1}$.

A number of mechanisms have been proposed for the bromide–polysulphide system under a range of conditions [25–31] including tribromide and polysulphide complexes, supersulphide radicals and intermediary steps. In this study a simple reaction mechanism is assumed:

$$Br_{2(aq)} + 2e^- \leftrightharpoons 2Br^- \quad (20)$$

$$S + 2e^- \leftrightharpoons S^{2-} \quad (21)$$

The kinetic data required for the model included rate constants and charge transfer coefficients. For the bromide couple, the rate constant was estimated from values of i_0 [20] to be 10^{-4}–$10^{-3}\ m\ s^{-1}$ on platinum electrodes [25,27] and 10^{-8}–$10^{-4}\ m\ s^{-1}$ on vitreous carbon electrodes [26,32]. No data is currently available for the bromide couple alone on activated carbon electrodes, but this is likely to be similar to vitreous carbon, *i.e.* a value in the range 10^{-6}–$10^{-8}\ m\ s^{-1}$ is reasonable. These authors also found a range of charge transfer coefficients from Tafel slopes, and it seems reasonable to use values for both α_a and α_c of 0.5.

For the sulphide/polysulphide couple, the rate constant on a range of metals including gold, tungsten, nickel, graphite, platinum and cobalt [29,33] has been estimated from i_0 values to vary in the range 10^{-10}–$10^{-7}\ m\ s^{-1}$ [20]. On activated carbon [34], the rate constant has been estimated to be $10^{-7}\ m\ s^{-1}$ [20]. Other studies found that the cathodic reaction had a high overpotential on gold [35], that α_a on graphite was 0.5 [36], and that the rate constant is 1st-order [37]. A range of charge transfer coefficients have been estimated, and it seems reasonable to use values for both α_a and α_c of 0.5.

A study of the PSB system as a whole on activated carbon found that the total overpotential for a PSB system at 40 $mA\ m^{-2}$, 299 K, 50% charged 4.0 M NaBr and 1.3 M Na_2S_4 electrolytes is 191 mV [7]. If half of this is assumed to be due to the membrane and electrolyte resistive losses [38], if the overpotential is assumed to caused by activation only, and if the bromide rate constant is assumed to be an order of magnitude greater than the sulphide rate constant (see Section 4), then $k_{s,Br}$ and $k_{s,S}$ can be estimated as 5×10^{-7} and $5 \times 10^{-8}\ m\ s^{-1}$ respectively.

4. Modelling the pilot-scale bromide–polysulphide system

A pilot-scale PSB RFB system was tested by Regenesys Technologies Ltd., and data from this system was used to validate the model. This system used a stack of 200 bipolar electrochemical cells, called the XL200.

4.1. Stack design

The XL cell considered in this paper had an electrode width and length of 66.8 and 108.0 cm respectively with a total projected area of 0.67 m^2. The electrode-membrane gap d_g averaged about 0.95 mm to give a flow cross-sectional area of 6.5 cm^2. The bipolar electrodes consisted of an electrically conductive, non-porous high-density polyethylene (HDPE)/graphite composite core on which particles of mixed polyvinylidene difluoride (PVDF) and activated carbon were compressed on both sides to increase the active surface area [39]. These electrodes were laser-welded into an HDPE frame and were about 5.5 mm thick. In the XL200 stack, 201 bipolar electrodes were aligned back-to-back to create 200 cells, each divided by a membrane 0.2 mm thick to give a total cell thickness of about 7.5 mm. The Nafion membrane material was assumed to have the properties of Nafion 117 (0.18 mm thick, and with a conductivity of 3 $S\ m^{-1}$ [40]). Each compartment contained a HDPE turbulence-promoting mesh to improve mixing. This mesh had a volumetric porosity of about 73%, a 45-degree cross pattern, a strand thickness of 0.45 mm and an overall thickness of about 0.90 mm. The XL200 stack was bounded by two mild steel endplates coated with resin and 80 cm wide, 155 cm tall and 4 cm thick, each containing a current feeder. Electrolytes were fed to the cells *via* 2.5-in. internal diameter chambers formed by the manifolds of the electrode frames, and through spirals in the manifolds included to reduce shunt currents. The electrolytes were then returned to large storage tanks where mixing with uncharged electrolyte occurred. A heat exchanger was included on the less-corrosive sulphide line, which maintained the electrolyte temperature at around 35 °C.

4.2. Flow conditions and mass transport

The variation in the mass transfer coefficient for the bromide compartment of an XL5 module (an XL200 module with 5 cells) has been found to be [39]:

$$Sh = 0.081 Re^{0.89} Sc^{0.33} \quad (22)$$

for 20 < Re < 120, where the Sherwood number Sh is $k_m d_e/D$, the Reynolds number Re is $v d_e/\nu$ and the Schmidt number Sc is ν/D. The hydraulic diameter d_e was 1.9 mm. The relationship for the slightly larger sulphide compartment (valid for 20 < Re < 150) was [41]:

$$Sh = 0.099 Re^{0.69} Sc^{0.33} \quad (23)$$

In this study, the average electrolyte velocity v was fixed at 25 $mm\ s^{-1}$ (a typical value for the XL200 [19]) for which Re_{Br} and Re_S were 62 and 46. The diffusion coefficients of the PSB system were estimated to be $12 \times 10^{-6}\ cm^2\ s^{-1}$ (bromine), $5 \times 10^{-6}\ cm^2\ s^{-1}$ (bromide), $6 \times 10^{-6}\ cm^2\ s^{-1}$ (sulphide) and $5 \times 10^{-6}\ cm^2\ s^{-1}$ (sulphur) [20].

4.3. Species concentrations

The concentrations of the oxidised (S and Br_2) and reduced (S^{2-} and Br^-) were calculated on each side of the membrane. The effect of electro-osmosis of water and self-discharge due to sulphide cross-over were included.

Cations crossed the cation-permeable membrane during charge cycles to maintain electro-neutrality, dragging with them associated water molecules that resulted in significant electrolyte volume fluctuations. Cations crossed from the bromide to the sulphide compartment on charge (decreasing V_{Br} and increasing V_S), and returned on discharge. Sodium ions were far likelier than hydrogen ions to be the main charge carrier in the PSB system due to its substantially higher concentrations and the preference of Nafion

membranes for sodium ions [40]. The transference coefficient of water t_{H_2O} was taken as 10 molecules of water per cation for Nafion 117 carrying pure sodium ions [40].

Self-discharge occurs due to sulphide ions crossing the membrane and reacting with bromine molecules:

$$HS^- + 4Br_2 + 4H_2O \leftrightharpoons {SO_4}^{2-} + 8Br^- + 9H^+ \quad (24)$$

This self-discharge results in decay of the equilibrium potential, and a simple estimate of the decay rate was by differentiating the Nernst equation for the PSB system:

$$\frac{dE_{eqm}}{dt} = \frac{RT}{2F}\left(\frac{1}{[Br_2]}\frac{d[Br_2]}{dt} + \frac{1}{[S^{2-}]}\frac{d[S^{2-}]}{dt} - \frac{2}{[Br^-]}\frac{d[Br^-]}{dt} - \frac{1}{[S]}\frac{d[S]}{dt}\right) \quad (25)$$

The rates of change of concentration were estimated from the fluxes of the four species across the membrane and from the resulting reactions that occurred:

$$\frac{d[Br_2]}{dt} = \frac{NA}{V_{Br}}(-4J_{S^{2-}} - J_{Br_2}) \quad (26)$$

$$\frac{d[Br^-]}{dt} = \frac{NA}{V_{Br}}(+8J_{S^{2-}} - J_{Br^-}) \quad (27)$$

$$\frac{d[S]}{dt} = \frac{NA}{V_S}(-J_S) \quad (28)$$

$$\frac{d\left[S^{2-}\right]}{dt} = \frac{NA}{V_S}\left(-J_{S^{2-}} - \frac{1}{4}J_{Br_2}\right) \quad (29)$$

There is no evidence that zero-valent sulphur crosses the membrane in significant amounts. The diffusion coefficient of molecular bromine through a cation exchange membrane with a water solvent was found to be 2.3×10^{-8} cm^2 s^{-1} [42], for which the resulting bromine flux was 1.15×10^{-9} mol cm^{-2} s^{-1} for a membrane thickness of 0.2 mm and a bromine concentration of 1.0 M. The flux of bromide ions across a Nafion 115 membrane has been found to be 3.6×10^{-9} mol cm^{-2} s^{-1} [41]. However, these fluxes were considered to be negligible compared to the sulphide flux. Substituting Eqs. (26)–(29) into Eq. (25), the sulphide flux across the membrane was found from the voltage decay rate:

$$J_{S^{2-}} = \frac{1000}{NA((1/[S^{2-}]_T V_S) + (4/[Br_2]_T V_{Br}) + (16/[Br^-]_T V_{Br}))}\frac{2F}{RT} \times \frac{dE_{eqm}}{dt} \quad (30)$$

Experimental studies have shown that the long-term decay for an XL200 stack in open-circuit potential can be taken as roughly constant at about 1.5×10^{-6} V s^{-1} cell^{-1} [20]. Taking the open-circuit voltage to be equivalent to the equilibrium voltage, the resulting sulphide flux was predicted to vary significantly during charge with an expected maximum value of 38×10^{-9} mol cm^{-2} s^{-1} (this was an order of magnitude larger than the bromide and bromine fluxes given above, confirming that the sulphide flux was dominant).

The changes in species concentration along the electrode were found from the applied current and sulphide flux as follows:

$$[Br_2]_{h+1} = [Br_2]_h + \frac{A_h}{1000\nu A_{Chan}}\left(\pm\frac{1}{2}\frac{i_h}{F} - 4J_{S^{2-}}\right) \quad (31)$$

$$[Br^-]_{h+1} = [Br^-]_h + \frac{A_h}{1000\nu A_{Chan}}\left(\pm\frac{i_h}{F} + 8J_{S^{2-}}\right) \quad (32)$$

$$[S]_{h+1} = [S]_h + \frac{A_h}{1000\nu A_{Chan}}\left(\pm\frac{1}{2}\frac{i_h}{F}\right) \quad (33)$$

$$[S^{2-}]_{h+1} = [S^{2-}]_h + \frac{A_h}{1000\nu A_{Chan}}\left(\pm\frac{1}{2}\frac{i_h}{F} - J_{S^{2-}}\right) \quad (34)$$

The variation of the tank electrolyte concentration and volume were found by numerical integration of the differential material balance equations.

4.4. Numerical optimisation and accuracy

The key numerical parameters in the model are the time step Δt, the number of electrode segments H, and the convergence criteria λ_h and λ_e. Decreasing the size of time step Δt had a 4th-order effect on numerical accuracy (see Fig. 3), as expected since Simpson's rule was used to calculate time-averaged quantities. At low values of Δt rounding errors prevented further improvement in the

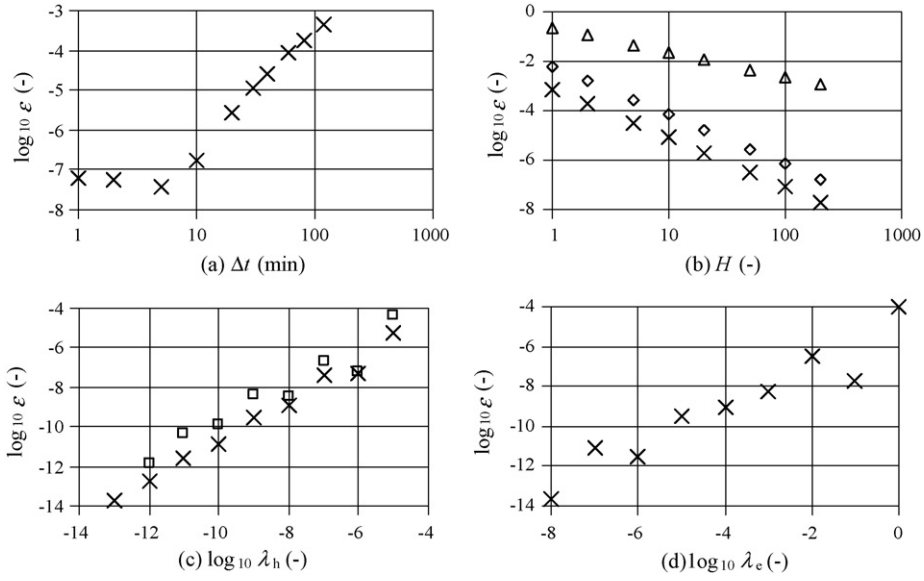

Fig. 3. Effect of numerical parameters on estimated relative error in performance measure: (×) π, (◊) $E_{dis,f}$, (□) $i_{dis,entry,f}$ and (△) $i_{dis,exit,f}$. Unless specified otherwise, $\Delta t = 1$ min, $H = 10$, $\lambda_h = 1 \times 10^{-6}$ V and $\lambda_e = 1 \times 10^{-3}$ A m^{-2}.

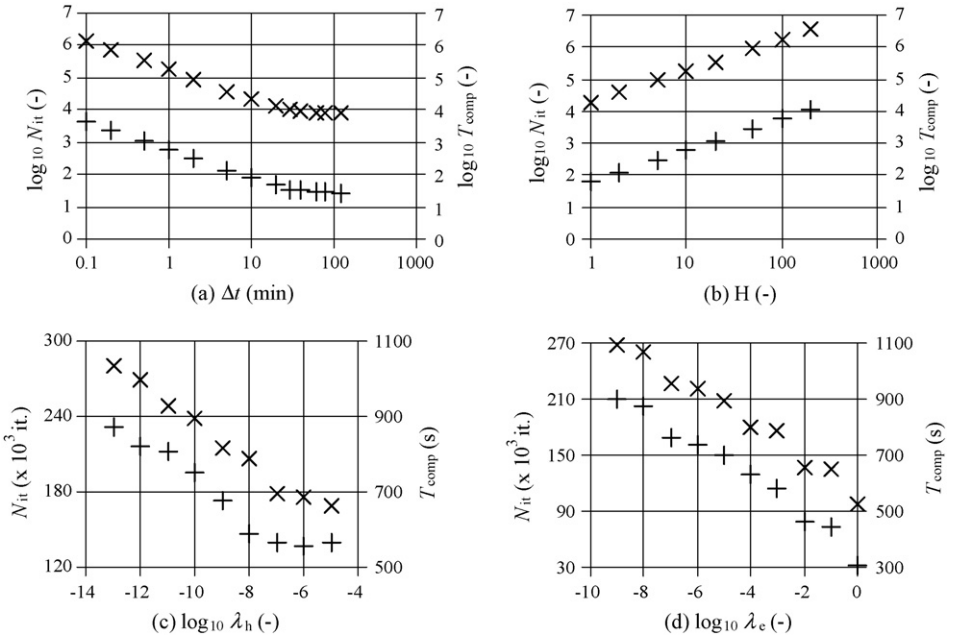

Fig. 4. Effect of numerical parameters on computational effort: (×) N_{it}, (+) T_{comp}. Numerical parameters as specified in Fig. 3.

accuracy. Increasing the number of electrode segments H had a 2nd-order effect on accuracy, while the current and voltage convergence criteria λ_h and λ_e had 1st-order effects.

The numerical parameters also affected computational effort. Computational cost was evaluated by recording the total number of iterations required for convergence and the computational time required to run the model in Visual Basic on a Dell Optiplex GX620 computer with a Pentium 4, 3.2 GHz processor and 1024 Mb of RAM. As can be seen in Fig. 4, the time step Δt and the number of segments H had approximately 1st-order effects on the number of iterations and modelling time required. Iteration convergence criteria had little effect on computational effort with power law exponents for λ_h and λ_e of only 0.03 and 0.05 respectively.

This information is summarised in Table 1. Also shown are the values of Δt, H, λ_h and λ_e selected on the basis of good numerical accuracy without excessive computational time. Numerical errors in integral quantities such as plant efficiency were limited to 10^{-4}, with the error for segment current density around 10^{-2}.

5. Results and discussion

The model's results were compared against two sets of experimental data for an XL200 stack to investigate the model's ability to reproduce observed behaviour under different operating conditions.

Table 1
Orders of effect of numerical parameters on model accuracy and values required to limit relative numerical error to 10^{-4}. Numerical parameters as specified in Fig. 3.

	Δt	H	λ_h	λ_e
Final discharge voltage	0	2nd	1st	1st
Final entry/exit discharge current density	0	1st	1st	1st
Energy efficiency π	3rd–4th	2nd	1st	1st
Computational time	0.9	1st	0.03	0.05
Total number of iterations	0.9	1st	0.03	0.05
Value to limit numerical error to 1×10^{-4}	24 time intervals	30	1×10^{-6} V	1×10^{-3} A m^{-2}

5.1. Six-cycle series charged at 600 A m^{-2}

The first set of experimental data consisted of six consecutive cycles charged for 65 min and discharged for 60 min at a current density of 600 A m^{-2}. During each changeover the stack was held under open-circuit conditions for 10 min to allow the voltages to stabilise. A summary of the parameters used to model this series of XL200 PSB cycles is given in Table 2. A detailed discussion of the selection of these parameters can be found elsewhere [20].

Fig. 5 shows the predicted voltage profile obtained from the model, along with the experimental voltage trace recorded for a working XL200 PSB system. The model results agreed well with the experimental data in a number of ways. In particular, the average value of the energy efficiency was calculated as 59.14 and 59.16% for the model and experiment respectively [20]. Both the actual and predicted open-circuit voltages decayed over time at similar rates due to self-discharge, and by the end of the series the system was very near to mass-transport limits as can be seen by the

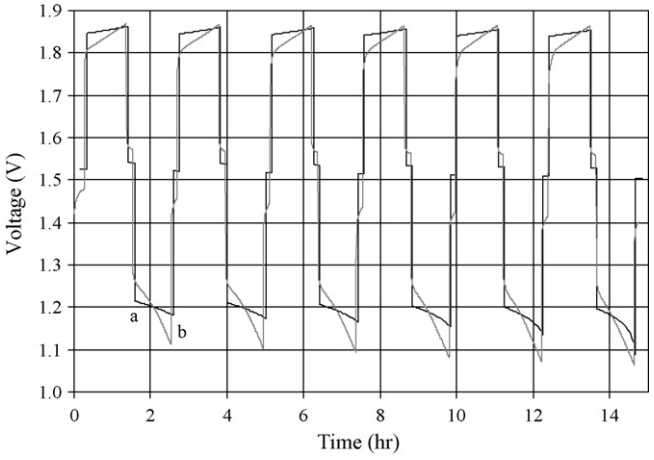

Fig. 5. Predicted and recorded cell voltage for a six-cycle series of an XL200 PSB system with the input data given in Table 2: (a) predicted voltage and (b) recorded voltage.

Table 2
Battery design used for modelling a series of 6 consecutive PSB cycles charged at 400 A m^{-2}.

System properties	Symbol (unit)	Value
Electrolyte velocity	v (mm s^{-1})	25
Number of cells	N (cells)	200
Transference coefficient	t	10 molecules H_2O per Na^+ ion transferred
OCV voltage decay rate	(V s^{-1} cell^{-1})	5×10^{-7}

Half-cycle properties		Charge	Discharge
Applied current density	i_{ch}/i_{dis} (A m^{-2})	600	600
Cycle length	t_{ch}/t_{dis} (min)	65	60

Half-cell properties		System A	System B
Oxidised/reduced on charge	–	Oxidised	Reduced
Standard redox potential	E^0 (V)	+1.09	−0.48
Kinetic rate constant	k_s ($\times 10^{-8}$ m s^{-1})	40	3
Initial electrolyte volume	V_0 (m^3)	3.5	3.5
Electrolyte viscosity	ν ($\times 10^{-6}$ m^2 s^{-1})	0.76	1.04
Initial state of charge	σ_I	0.3	0.19
Mass transport relationship	–	$Sh = 0.081 Re^{0.89} Sc^{0.333}$	$Sh = 0.099 Re^{0.69} Sc^{0.333}$

Species properties		Bromine	Bromide	Sulphur	Sulphide
Stoichiometric coefficient	z	1	2	1	1
Diffusion coefficient	D ($\times 10^{-10}$ m^2 s^{-1})	20	12	5	6
Initial electrolyte concentrations	[P] (M)	0.73	3.42	2.86	1.53

Electrolyte properties		System A	System B	Membrane
Conductivity	κ (S m^{-1})	23	29	1
Thickness	l (mm)	0.95	0.95	0.2

sharp drop-off in cell voltage towards the end of discharge. There were also a number of differences in the data. The predicted voltage changed more slowly during half-cycles (especially on charge). This could be because side reactions such as gas evolution were ignored and the model could not exceed mass-transport limits. The model over-predicted cell voltage on charge, and this is probably due to the use of the same rate constant for both forward and reverse reactions. The model open-circuit voltage stabilised immediately as capacitance effects and the time taken to reach equilibrium were neglected.

The predicted variation in species concentration in the electrolyte tanks is shown in Fig. 6. The rate of change of concentration varied during half-cycles due to the varying cross-membrane sulphide flux and the change in electrolyte volume (due to the electro-osmotic water flux). The concentration of Br_2 decreased and the Br^- concentration increased during the series of cycles due to a combination of self-discharge and the net transfer of water to the sulphide electrolyte as the duration of the charge cycle t_{ch} was longer than the discharge cycle t_{dis}. Over the series of cycles, the concentration of S^{2-} fell slightly due to the sulphide flux through the membrane, and the zero-valent sulphur concentration also fell slightly due to the longer charge period.

The resulting variation in the state of charge is shown in Fig. 7. Both σ_S and σ_{Br} increased on charge and decreased on discharge, but neither electrolyte used its full state of charge range. The value σ_{Br} was limited in order to minimise the risk of corrosion and Br_2 release. The initial value of σ_{Br} was selected to ensure that it did not decrease to zero due to self-discharge. Greater utilisation of the sulphide electrolyte could be achieved by reducing the electrolyte volume; the resulting higher species concentrations would improve mass transport, and smaller electrolyte and tank costs would be required. The fluctuation of σ_S during cycles was less than that of σ_{Br} due to the greater amount of total sulphur in solution. Even

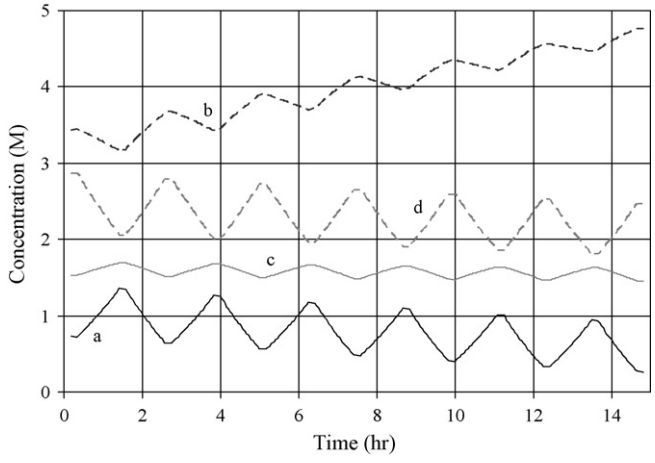

Fig. 6. Predicted variation in electrolyte tank concentrations for a six-cycle series of an XL200 PSB system with the input data given in Table 2: (a) [Br_2], (b) [Br^-], (c) [S^{2-}] and (d) [S].

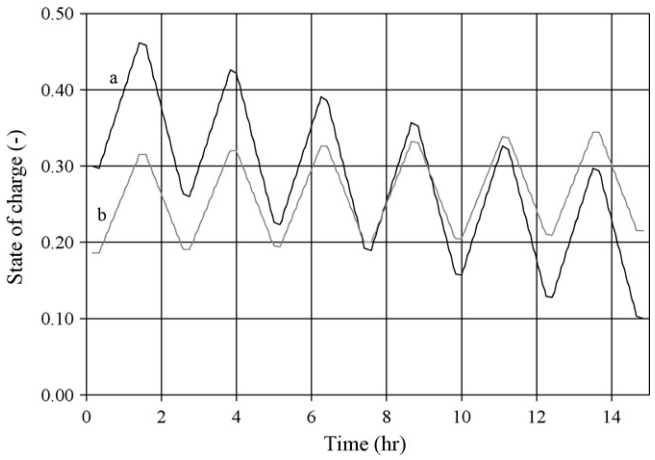

Fig. 7. Predicted variation in state of charge for a six-cycle series of an XL200 PSB system with the input data given in Table 2: (a) σ_{Br} and (b) σ_S.

though the duration of the charge cycle t_{ch} exceeded the discharge cycle t_{dis}, the bromide state of charge σ_{Br} decreased with each cycle due to the sulphide flux. Conversely the sulphide state of charge σ_S rose slightly over time due to a decrease in the concentration of zero-valent sulphur.

The predicted variation in the current density is shown in Fig. 8 at a number of locations along the electrode. The current density was lower at the electrode outlet than at the inlet due to the lower concentrations of reactant. The range of current density variation along the electrode increased during half-cycles as the conversion per pass increased, increasing the mass transport overpotential and hence reducing the local current density at the outlet. The range of current densities was also larger on discharge than on charge as the system was closer to mass transport limiting conditions. This range of current densities on discharge increased each cycle as the bromide side state of charge decreased leading to increasing mass transport overpotentials at the cell outlet.

The predicted variation in the dimensionless current density, i_d (the ratio of current density to limiting current density), is shown in Fig. 9. As expected, the current density at the exit is closer to mass transport limiting conditions than at the inlet. During each half-cycle, i_d increased as the limiting current decreased with reactant concentrations. For most of the six-cycles, the current density was always less than 50% of the limiting current. However, during the last few cycles, limiting conditions are approached at the end of discharge on the bromide side. This led to high overpotentials and reduced efficiency, and consequently the experiment was terminated.

5.2. Seventeen-cycle series charged at 400 A m^{-2}

A series of 17 consecutive charge–discharge cycles was also studied. This series began with 3.8 and 3.2 m^3 of fresh bromide and sulphide electrolytes respectively, and the initial species concentrations were 4.5 M Br^-, 3.8 M S and 1 M S^{2-}. For modelling purposes, the initial Br_2 concentration was assumed to be 10^{-4} M as zero concentrations are incompatible with the Nernst equation. The charge and discharge current densities were 400 and 600 A m^{-2} respectively. For the first cycle the charging time was 175 min, and for subsequent cycles it was 110 min. The discharge time was 65 min for each cycle except for the twelfth cycle, for which 58.5 min was used for balancing purposes. Between each changeover the stack was held under open-circuit conditions for 10 min to allow the voltage to stabilise.

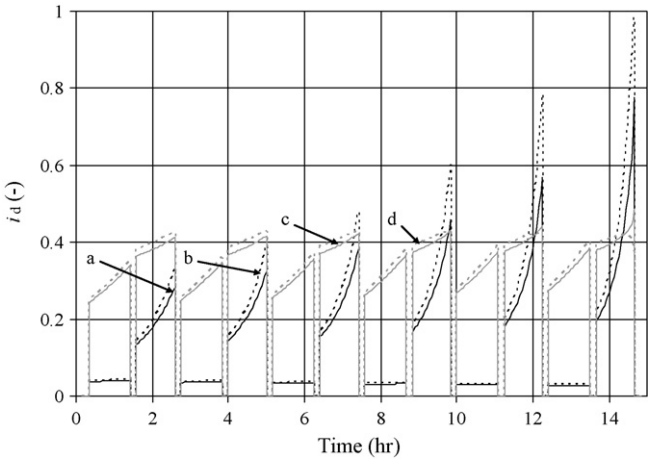

Fig. 9. Predicted variation in dimensionless current $i_d = i/i_L$ for a six-cycle series of an XL200 PSB system with the input data given in Table 2: (a) $i_{d,Br,entry}$, (b) $i_{d,Br,exit}$, (c) $i_{d,S,entry}$ and (d) $i_{d,S,exit}$.

For the model, lower rate constants $k_{s,Br}$ and $k_{s,S}$ of 10^{-7} and 10^{-8} m s^{-1} respectively were selected in order to avoid discontinuities in overpotential occurring at the transition point between linear and Tafel approximations to the Butler-Volmer equation [20]. It was not possible to achieve a current density on discharge of 600 A m^{-2} without exceeding limiting current conditions. It was therefore assumed that a constant current efficiency of 93.3% was achieved (*i.e.* a discharge current density of 560 A m^{-2} was applied in the model). A lower OCV decay rate of 4×10^{-7} V s^{-1} cell^{-1} was used in order to prevent species concentrations falling to zero over the 17-cycle series. A membrane conductivity of 3 S m^{-1} was used; other model settings were as given in Table 2.

The resulting model cell voltage is shown in Fig. 10 along with the experimental cell voltage data for comparison. The model overestimated the voltage during charging, probably due to the low rate constant used. Conversely on discharge the cell voltage was underestimated due to the lower discharge current density. The predicted rate of change of voltage during half-cycles was also lower than the observed rate. Nevertheless the agreement was good in several aspects. In particular the sharp drop-off in cell voltage on discharge was observed in both the model and experimental data due to mass transport overpotentials. The experimental data indicated that higher mass transport overpotentials occurred than

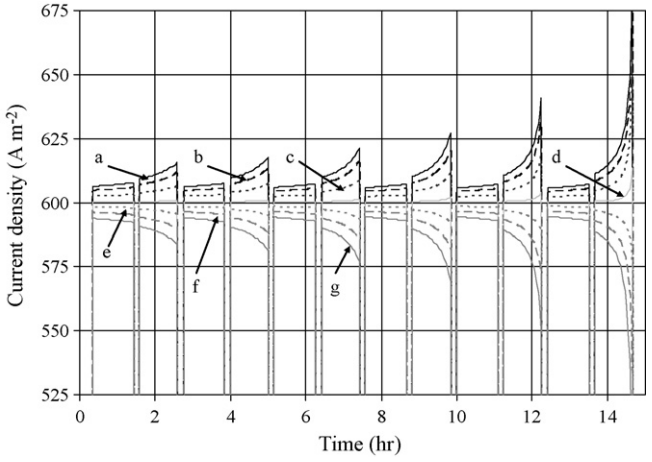

Fig. 8. Predicted variation in current density distribution for a six-cycle series of an XL200 PSB system with the input data given in Table 2: (a) entry segment, (b) 5th, (c) 10th, (d) 15th, (e) 20th, (f) 25th and (g) exit segment.

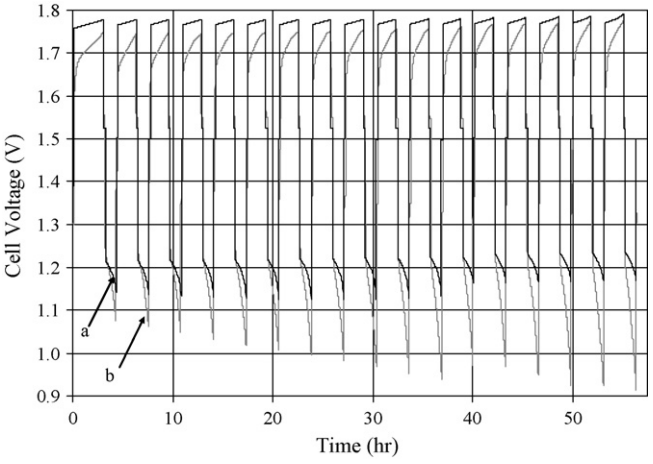

Fig. 10. Predicted and recorded variation in cell voltage for a 17-cycle series of an XL200 PSB with the input data specified in Section 4.2: (a) predicted voltage and (b) recorded voltage.

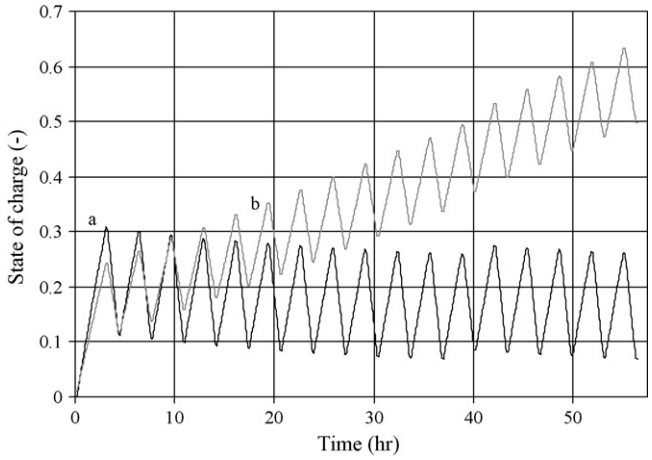

Fig. 11. Predicted variation in state of charge for a 17-cycle series of an XL200 PSB with the input data specified in Section 4.2: (a) σ_{Br} and (b) σ_S.

those predicted by the model. Simulations of the cell voltages close to mass transport limiting conditions were found to be very sensitive to the applied current. The shorter discharge period on cycle 12 was used to increase the average state of charge and hence reduce mass-transport limits overpotentials during discharge. Although the effect of this shorter cycle in later cycles is evident in the model results, it is less clear in the experimental data.

The predicted variation in state of charge is shown in Fig. 11. On the bromide side, σ_{Br} cycled roughly between 0.1 and 0.3 throughout the series as the loss of bromine due to the sulphide flux was counterbalanced by the net excess of bromine resulting from the greater amount of charge stored on charge than was recovered on discharge. The low state of charge on the bromide side is associated with the high mass transport overpotentials at the end of discharge as the Br_2 concentration falls. On the sulphide side, σ_S steadily increased during the series due to the decay in [S]. Towards the end of the 12 cycles, mass transport overpotentials are evident at the end of charge, due to decreasing concentrations of zero-valent sulphur.

The predicted variation in i_d is shown in Fig. 12. On the bromide side, $i_{d,Br}$ was very low during charge throughout the series due to the high concentrations of bromide. On discharge $i_{d,Br}$ was very high, frequently exceeding 0.9 at the electrode exit. This confirms that the rapidly decreasing potentials at the end of discharge are due

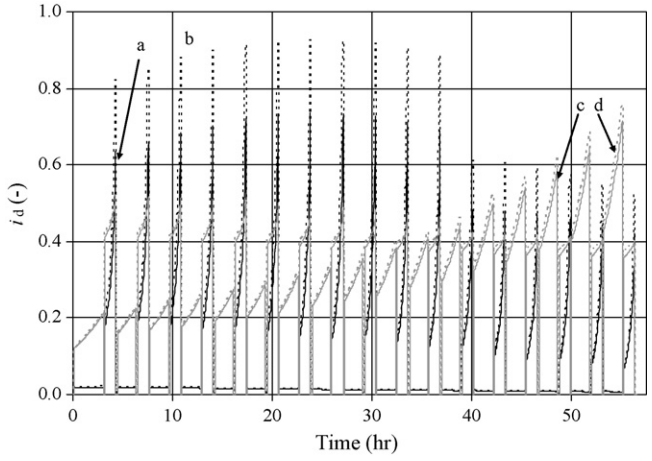

Fig. 12. Predicted variation in dimensionless current i_d for a 17-cycle series of an XL200 PSB with the input data specified in Section 4.2: (a) $i_{d,Br,entry}$, (b) $i_{d,Br,exit}$, (c) $i_{d,S,entry}$ and (d) $i_{d,S,exit}$.

to increasing mass transport overpotentials at the bromide electrode. After cycle 12 $i_{d,Br}$ rarely exceeded 0.6 as the shorter discharge period moved the system away from mass-transport limits.

On the sulphide side, $i_{d,S}$ was initially higher on discharge than on charge due to relatively low sulphide concentrations. Over time, $i_{d,S}$ became higher on charge due to falling concentrations of zero-valent sulphur. Again, this confirms that mass transport overpotentials occur during charging in later cycles at the sulphide electrode.

6. Conclusions

This study has shown that modelling of redox flow battery systems for energy storage can reveal important characteristics and loss mechanisms over a series of cycles under different operating conditions. For example, for the conditions studied, mass transport overpotentials at the bromide electrode were found to limit the performance during discharge. Enhancement of mass transport coefficients in the bromide electrolyte may be recommended. The model showed that significant drift in conditions could occur due to self-disharge and electro-osmotic effects. Careful electrolyte management will be required for reliable operation of the PSB RFB system. The model can also be used to find suitable electrochemical rate constants by fitting with experimental data. For the PSB system at the composite activated carbon electrodes developed by Regenesys, bromide and sulphide rate constants of 4×10^{-7} and 3×10^{-8} m s^{-1} were obtained. In a following paper [18] we show how the model can be used for design and optimisation of a large scale RFB system.

Acknowledgements

The authors are grateful to Regenesys for the provision of the experimental data. They are also grateful to Regenesys and the EPSRC for funding provided for the research.

References

[1] M. Bartolozzi, J. Power Sources 27 (1989) 219–234.
[2] C. Ponce de Leon, A. Frias-Ferrer, J. Gonzalez-Garcia, D. Szanto, F. Walsh, J. Power Sources 160 (2006) 716–732.
[3] EPRI-DOE Handbook of Energy Storage for Transmission and Distribution, EPRI and the US Department of Energy, 2003, 1001834.
[4] VRB Power Acquires Regenesys Electricity Storage Technology, 5th October 2004, URL: <http://powerelectronics.com/news/vrb-power-regenesys> (Accessed October 2008).
[5] A. Price, S. Bartley, S. Male, G. Cooley, Power Eng. J. 13 (1999) 122–129.
[6] P. Zhao, H. Zhang, H. Zhou, B. Yi, Electrochim. Acta 51 (2005) 1091–1098.
[7] H. Zhou, H. Zhang, P. Zhao, B. Yi, Electrochim. Acta 51 (2006) 6304–6312.
[8] E. Sum, M. Skyllas-Kazacos, J. Power Sources 15 (1985) 179–190.
[9] M. Skyllas-Kazacos, Vanadium Geol. Proc. Appl. Com 2002 (2002) 63–78.
[10] M. Skyllas-Kazacos, J. Power Sources 124 (2003) 299–302.
[11] High capacity electrical storage, URL: <http://pluronsystems.com> (Accessed October 2008).
[12] B. Fang, S. Iwasa, Y. Wei, T. Arai, M. Kumagai, Electrochim. Acta 47 (2002) 3971–3976.
[13] A. Paulenova, S. Creager, J. Navratil, Y. Wei, J. Power Sources 109 (2002) 431–438.
[14] P. Fedkiw, R. Watts, J. Electrochem. Soc. 131 (1984) 701–709.
[15] N. Koshel, V. Zvychainyi, Russ. J. Electrochem. 33 (1997) 904–909.
[16] R. White, S. Lorimer, J. Electrochem. Soc. 130 (1983) 1096–1103.
[17] T. Evans, R. White, J. Electrochem. Soc. 134 (1987) 2725–2733.
[18] D.P. Scamman, G.W. Reade, E.P.L. Roberts, J. Power Sources (2009), doi:10.1016/j.jpowsour.2009.01.076, in press.
[19] A. Bard, L. Faulkner, Electrochemical Methods, John Wiley & Sons, New York, 1980.
[20] D. Scamman, EngD Thesis, University of Manchester, Manchester, 2007.
[21] Gould Laboratories, J. Power Sources 5 (1980) 353–354.
[22] P. Singh, B. Jonshagen, J. Power Sources 35 (1991) 405–410.
[23] S. Licht, J. Electrochem. Soc. 134 (1987) 2137–2141.
[24] S. Licht, J. Davis, J. Phys. Chem. 101 (1997) 2540–2545.
[25] G. Faita, G. Fiori, T. Mussini, Electrochim. Acta 13 (1968) 1765–1772.
[26] M. Mastragostino, C. Gramellini, Electrochim. Acta 30 (1985) 373–380.
[27] I. Rubinstein, J. Phys. Chem. 85 (1981) 1899–1906.

[28] P. Lessner, J. Winnick, F. McLarnon, E. Cairns, J. Electrochem. Soc. 133 (1986) 2517–2522.
[29] P. Lessner, F. McLarnon, J. Winnick, E. Cairns, J. Electrochem. Soc. 134 (1987) 2669–2676.
[30] S. Licht, Nature 330 (1987) 148–151.
[31] S. Licht, J. Electrochem. Soc. 135 (1988) 258–259.
[32] I. Vogel, A. Mobius, Electrochim. Acta 36 (1991) 1403–1408.
[33] P. Allen, A. Hickling, Trans. Faraday Soc. 53 (1957) 1626–1635.
[34] T. Calver, S. Male, P. Mitchell, I. Whyte, GB Patent 2337150 (1999).
[35] A. Ahern, L. Burke, D. Casey, P. Morrissey, Electrochem. Soc. Proc. 23 (2001) 174–185.
[36] Q. Yi, Q. Chen, J. Zhou, P. Zhang, Trans. Nonferrous Met. Soc. China 10 (2000) 534–537.
[37] S. Shmakov, M. Tarasevich, A. Dribinskii, V. Rylov, Elektrokhimiya 25 (1989) 376–382.
[38] D. Genders, Regenesys: a large scale energy storage system, Electrochem. (2003), Southampton, UK.
[39] C. Ponce-de-Leon, G. Reade, I. Whyte, S. Male, F. Walsh, Electrochim. Acta 52 (2007) 5815–5823.
[40] T. Okada, S. Moller-Holst, O. Gorseth, S. Kjelstrup, J. Electroanal. Chem. 442 (1998) 137–145.
[41] C. Ponce de Leon, F. Walsh, Summary of Bath University R&D activities using the XL5 modular redox flow cell May–July 2003, University of Bath, Report No. QRB2/03, 2003.
[42] A. Heintz, C. Illenberger, J. Membr. Sci. 113 (1996) 175–181.